

Alignment-Optimised Coaxial Visible-NIR-II Dual-Channel Surgical Navigation System and Its Clinical Application in Blood-Supply Assessment

Zhang Yu-Huang¹, Liu Xiao-Long², Sun Si-Ying¹, Fan Xiao-Xiao², Lin Hui², Qian Jun^{1*}

- (1. Centre for Optical and Electromagnetic Research, College of Optical Science and Engineering, International Research Center for Advanced Photonics, Zhejiang University, Hangzhou 310058, China;
2. Department of General Surgery, Sir Run Run Shaw Hospital, School of Medicine, Zhejiang University, Hangzhou, 310058, China)

Abstract: Fluorescence imaging in the second near-infrared window (NIR-II, 900-1880 nm) offers high signal-to-background ratio (SBR), enhanced definition, and superior tissue penetration, making it ideal for real-time surgical navigation. However, with single-channel imaging, surgeons must frequently switch between the surgical field and the NIR-II images on the monitor. To address this, a coaxial dual-channel imaging system that combines visible light and 1100 nm longpass (1100LP) fluorescence was developed. The system features a customized coaxial dual-channel lens with optimized distortion, achieving precise alignment with an error of less than ± 0.15 mm. Additionally, the shared focusing mechanism simplifies operation. Using FDA-approved indocyanine green (ICG), the system was successfully applied in dual-channel guided rat lymph node excision, and blood supply assessment of reconstructed human flap. This approach enhances surgical precision, improves operational efficiency, and provides a valuable reference for further clinical translation of NIR-II fluorescence imaging.

Key words: NIR-II, dual-channel, fluorescence imaging, surgical navigation, coaxial

PACS:

精准对齐的共轴可见光-近红外二区双通道手术导航系统及其在临床人血供评估中的应用

张浴煌¹, 刘孝龙², 孙思颖¹, 樊潇霄², 林辉², 钱骏^{1*}

- (1. 浙江大学光电科学与工程学院光及电磁波研究中心 先进光子学国际研究中心, 浙江 杭州, 310058;
2. 浙江大学医学院附属邵逸夫医院 普外科, 浙江 杭州, 310058)

摘要: 在近红外二区 (the second near-infrared window, NIR-II, 900-1880 nm) 的荧光成像具有高信号背景比、高清晰度和优秀的组织穿透能力, 是实时手术导航的理想选择。然而, 对于单通道成像, 外科医生不得不经常在手术区域和显示器上的 NIR-II 图像之间切换观察。为此, 开发了一种共轴双通道成像系统, 它可同时对可见光和 1100 nm 长通的荧光成像。该系统采用定制的共轴双通道镜头并优化了畸变, 实现了通道间图像的精确对齐, 所测得的误差均小于 ± 0.15 mm。此外, 两通道共用了对焦镜组, 因而简化了对焦操作。结合使用美国食品及药物管理局批准的吲哚菁绿为探针, 成功实现了双通道导航的大鼠淋巴结切除和临床上对重建后皮瓣的血供恢复情况的评估。这种方法能让手术更为精准和高效, 并为 NIR-II 荧光成像的进一步临床转化提供有价值的参考。

关键词: 近红外二区; 双通道; 荧光成像; 手术导航; 共轴光路

中图分类号: O43

文献标识码: A

Foundation items: the National Natural Science Foundation of China (U23A20487); the National Key R&D Program of China (2022YFB3206000); Dr. Li Dak Sum & Yip Yio Chin Development Fund for Regenerative Medicine, Zhejiang University; the National Natural Science Foundation of China (61975172).

Biography: Zhang Yu-Huang (1994-), male, Hangzhou, Ph. D student. Research area involves NIR-II fluorescence imaging. E-mail: yuhuangzhang@zju.edu.cn

* **Corresponding author:** Qian Jun E-mail: qianjun@zju.edu.cn

Introduction

Fluorescence imaging is widely used in clinical surgery as a real-time navigation technique due to its ease of use and lack of ionizing radiation^[1-4]. Compared to visible light, fluorescence imaging in the near-infrared (NIR) window offers reduced scattering, better clarity, deeper tissue penetration, and a higher signal-to-background ratio (SBR), leading to its rapid adoption in various surgical procedures, including coronary angiography, tumor resection and lymph node clearance^[5-10]. The first near-infrared window (NIR-I, 700-900 nm) was initially used, as it can be detected with mature silicon-based cameras. However, many biological tissues, such as liver and intestine, emit bright autofluorescence in this range, which can seriously interfere with target detection^[11]. Besides, the limit definition and penetration depth of NIR-I imaging are insufficient to meet the demands of bioimaging applications^[12, 13].

In recent years, fluorescence imaging has expanded to the second near-infrared window (NIR-II, 900-1880 nm), significantly enhancing image clarity and tissue penetration while greatly reducing autofluorescence to nearly absent levels^[13-19]. NIR-II technology allows for more precise identification of lesions, enabling their complete removal with minimal damage to surrounding normal tissue, thus supporting for more precise surgery^[20-22]. Nowadays, NIR-II fluorescence imaging has been successfully applied in some clinical settings for liver tumors, gliomas, and orthopedic surgeries, enhancing surgical efficiency and patient outcomes^[12, 23-25].

However, surgeons often need to switch between the NIR-II image on the monitor and the surgical field, and correlate fluorescent regions with anatomical structures. This frequently switching decreases operational efficiency and complicates delicate procedures^[26]. A simple solution is to develop a dual-channel imaging system that combines visible and NIR-II imaging. Early systems placed visible and NIR-II imaging units side by side, but this non-coaxial setup introduced parallax^[23]. Our previous work achieved coaxial imaging using a dichroic mirror and separate lenses, which eliminated parallax but faced challenges in aligning the two channels across the entire field of view due to different distortions of the lenses. Additionally, the separate focusing mechanisms complicated the operation^[27].

In this work, we demonstrate the significant advantage of 1100 nm longpass (1100LP) fluorescence imaging in terms of SBR over the NIR-I window. We developed an advanced coaxial dual-channel imaging system for visible light and 1100LP fluorescence. To achieve precise alignment of the two channels, we customized a lens with coaxial design and optimized lens distortion. The alignment error between the two channels was measured to be less than ± 0.15 mm. Moreover, the shared focusing lens simplifies the focusing process. Using the FDA-approved indocyanine green (ICG) dye as NIR-II

fluorescence probe, we were able to visualize liver and blood vessels as small as 0.44 mm in a rat through intact skin. In rat, dual-channel guided lymph node (LN) excision was successfully performed. The system allows the operator to quickly localize target and precisely resect. Finally, the system was used to assess the blood supply of a reconstructed human flap. The system helps to accurately assess the neovascularization and provides specific areas of necrotic foci. Our work provides a valuable reference for the clinical translation of NIR-II fluorescence imaging.

1 Experiments

1.1 Materials and animal handling

ICG used for animal experiments was purchased from Meilunbio and dissolved in deionized water before use. All animals were obtained from the Laboratory Animal Center of Zhejiang University. Female Sprague-Dawley rats (350 g) were used in all animal experiments, which were conducted under the approval of the Laboratory Animal Ethics Committee of Zhejiang University (Approval Number: ZJU20220283).

1.2 Comparison of imaging performance among visible light, NIR-I fluorescence, and 1100LP fluorescence

A 250 μ L solution of ICG (1 mg/mL) was administered via subcutaneous injection into one hind paw pad. After lymphatic uptake, ICG subsequently labeled the retroperitoneal LN. Visible light images were captured by a mobile phone's camera. NIR imaging was conducted using a lab-built NIR macroscopic fluorescence imaging system. This system incorporates a 690 nm continuous wave (CW) laser as the excitation light source. The laser beam, after collimation, undergoes lens expansion and diffusion through ground glass to produce a uniform illumination on the subject. Fluorescence was collected using an infrared antireflection lens (focal length: 35 mm, Tekwin, China) positioned above the subject. The collected light then passed through filters, and focused on the NIR camera sensor.

For NIR-I imaging, we employed a combination of 750 nm long-pass (LP) filter (FELH0750, Thorlabs, USA), a 900 nm short-pass (SP) filter (FESH0900, Thorlabs, USA), and a silicon-based camera (sensitivity range: 400-1100 nm, GA1280, Tekwin, China). The excitation light power density was set at 6 mW/cm², with an integration time of 2.5 ms.

For NIR-II imaging, we utilized a 1100 nm LP filter (FELH1100, Thorlabs, USA) and an InGaAs-based camera (sensitivity range: 900-1700 nm, 640 \times 512, SW640, Tekwin, China). The excitation light power density was set at 16 mW/cm², with an integration time of 50 ms.

1.3 Spectral measurements

ICG spectral measurements were performed using a lab-built spectral analysis system. Excitation light from a CW semiconductor laser was collimated and directed at the edge of a cuvette containing 0.1 mg/mL ICG solution. Fluorescence emitted from the ICG near the cuvette

wall was collected by a 25× objective (Olympus, Japan) and passed through filters to eliminate excitation light interference. The fluorescence was then coupled into a fiber by a collimator and transferred to a spectrometer for detection.

Due to the limited sensitivity range of a signal spectrometer, we analyzed the NIR-I and NIR-II spectra separately. For the NIR-I spectrum, we employed a 665 nm laser as the excitation light source, a 750 nm LP filter (FELH0750, Thorlabs, USA), and a visible-near-infrared spectrometer (sensitivity range: 360-1100 nm, PG2000, Ideaoptics, China). For the NIR-II spectrum, we used an 808 nm laser for excitation, a 950 nm LP filter (FELH0950, Thorlabs, USA), and a near-infrared spectrometer (sensitivity range: 900-2400 nm, NIR2200, Ideaoptics, China).

1.4 Construction of the coaxial visible and NIR-II imaging system

We developed a coaxial visible and NIR-II dual-channel imaging lens (focal length: 34 mm; f-number: $f/5$ for visible light and $f/3.2$ for NIR-II). The optical assembly primarily consists of a focusing lens group, a dichroic prism, and two lens groups for visible light and NIR-II light, respectively. The focusing lens group enable simultaneous focusing for both channels. The dichroic prism deflects visible light while transmitting NIR-II light. The visible and NIR-II lens groups are individually utilized for light focusing and aberration correction for each channel. In the design process, both channels were engineered to have the same magnification, with careful minimization of inter-channel distortion differences. This design allows for precise alignment of dual-channel raw images after simple processing, such as rotation, translation (to account for mechanical assembly errors), and scaling.

During imaging, excitation light from the laser is expanded and homogenized before illuminating the target. The visible and NIR-II light are then collected by the lens and separated into two paths. The visible light image is captured by an RGB camera (4096×2160, BIG-EYE10000KPA, ToupTek, China), while the NIR-II light passes through a 1100 nm LP filter before imaging on the SW640 camera. The entire system is mounted on a tripod for mobility. After capturing images from the two channels, image enhancement (Auto Level) was applied to the raw data. The NIR-II image was then converted from grayscale to RGB, where the NIR-II signal was assigned to the green channel. The brightness of both the visible light and NIR-II images was halved, and the intensities of the corresponding RGB channels were added together to create the merged image.

1.5 Dual-channel alignment error characterization

To characterize the alignment error of the dual-channel system, we imaged a ruler illuminated by a halogen lamp. The halogen lamp's emission spectrum includes NIR-II components, enabling NIR-II bright-field imaging. ImageJ was used to draw lines crossing the scales and obtain intensity profiles. MATLAB was employed to

normalize the two intensity curves and identify the positions of minima points less than 0.35. The distance between corresponding minima points in the two channels was considered as the alignment error of the dual channels.

1.6 Rat blood vessels imaging and dual-channel guided popliteal LN resection surgery

For rat blood vessels imaging, abdominal hair was removed one day prior to imaging. The rat was anesthetized and then intravenously injected with 500 μL of 2 mg/mL ICG solution. Excitation was provided by an 808 nm laser with a power density of 140 mW/cm^2 . The integration time for the NIR-II channel was set to 50 ms.

For popliteal LN resection, the hair around the rat's popliteal fossa was removed, followed by the injection of 250 μL of 1 mg/mL ICG solution into the hind paw pad. Under 808 nm excitation (20 mW/cm^2), the popliteal LN became visible in the 1100LP channel. Guided by the merged images, the LN was carefully excised.

1.7 Patient recruitment and clinical data collection

A patient with a degloving injury on the left foot dorsum, sustained in a car accident, was treated at Sir Run Run Shaw Hospital. Due to severe soft tissue contusion, the patient underwent thorough debridement followed by replantation of the degloved dorsal skin flap. During a follow-up examination one week after surgery, visual inspection revealed black necrosis at the flap's edge.

To assess blood supply recovery and identify areas of necrosis, an NIR fluorescence blood supply assessment was deemed necessary. After providing informed consent, the patient agreed to undergo this assessment with NIR-II fluorescence imaging, along with the collection of basic clinical information.

Following an intravenous injection of ICG (2.5 mg/mL, 3 mL), imaging was performed using the dual-channel system with 808 nm laser excitation. The NIR-II camera was positioned approximately 50 cm from the target, with no need to turn off ambient light. The integration time for 1100LP imaging was approximately 40 ms. Blood vessels in the dorsal foot began to appear 45 seconds post-injection approximately.

By integrating visible light with NIR-II fluorescence imaging, necrosis at the flap edge was accurately identified, leading to targeted debridement of necrotic skin and subcutaneous tissue. This study was approved by the Ethics Committee of Sir Run Run Shaw Hospital (Approval Number: 20220279).

2 Results and discussions

2.1 Comparison of visible light, NIR-I, and NIR-II fluorescence imaging

ICG is a widely used chromophore and fluorophore in clinical practices, such as choroidal angiography, lymphangiography, tumor surgery, and blood supply assessment^[12, 28-31]. Once ICG enters the vasculature, it could be rapidly metabolized by the liver^[32]. The emission peak wavelength of ICG in aqueous solution is approximately 835 nm, but there is also a considerable

emission tail in the NIR-II window that extends beyond 1100 nm (see Fig. 1a).

Figs. 1b-d clearly demonstrate the imaging advantages of 1100LP over the visible and NIR-I windows. A rat's retroperitoneal lymph node (LN) was labeled via injecting ICG solution into one hind paw pad, followed by capturing NIR-I and 1100LP fluorescence images under 690 nm light excitation. As shown in Fig. 1b, the LN is not visible in the visible light image as it is obscured by surrounding fat tissue. Although the NIR-I image presents LN's position and morphology (Fig. 1c), it also shows bright background autofluorescence from hair, cervix, and intestines, which might interfere with the identification of the labeled target. By contrast, the NIR-II fluorescence image only shows the LN in the entire field of view (Fig. 1d). Fig. 1e presents the intensity profiles along the dashed lines in Figs. 1c and d. The calculated SBRs are shown in Fig. 1f, with hair, cervix, and intestine as the backgrounds. The SBRs of LN in NIR-II image reaches as high as 13.07, with a minimum of 9.94, whereas in the NIR-I window, they are at most only 1.96.

2.2 Development of coaxial visible and NIR-II dual-channel imaging system

Two solutions were applied to minimize alignment errors between the visible and NIR-II imaging channels. Firstly, we customized a coaxial visible and NIR-II dual-channel imaging lens. This lens assembly includes focusing lens group shared by both channels, a dichroic prism for light splitting, and two imaging lens groups for each channel. The coaxial design in object space effectively eliminates parallax. Secondly, both channels of the lens were designed to have the same magnification, and the distortion differences between channels has been intentionally minimized, ensuring precise alignment across the entire field of view. Notably, the shared focusing lens group simplifies operation compared to separated focusing mechanisms.

Based on the lens, we constructed a coaxial dual-channel imaging system with visible and 1100LP windows (Fig. 2). The system employs RGB and InGaAs cameras for capturing the visible and NIR-II images, respectively. Figs. 3a and b show dual-channel images of a ruler under halogen illumination. By analyzing the ruler scales' overlap between the channels, we quantitatively assessed the system's alignment accuracy. The blue and red curves in Fig. 3c represent intensity profiles along the dashed lines in Figs. 3a and b, demonstrating precise overlap of all valleys caused by scale lines. The alignment errors between corresponding valleys of the two channels, indicated by the orange line in Fig. 3c, are all controlled within ± 0.15 mm, ensuring precise target positioning.

2.3 Visualization of live rat's liver and blood vessels through intact skin

A rat was intravenously injected with ICG solution after abdominal hair removal. Figs. 4a-c show the RGB, 1100LP, and merged images, respectively. The 1100LP image reveals abundant vascular details that are not visi-

ble in the RGB image. It resolves small blood vessels with a full width at half maximum (FWHM) of only 0.44 mm, demonstrating its high spatial resolution (see Fig. 4d). Additionally, despite being obscured by thick skin, the boundaries of the ICG-accumulated liver can still be clearly observed. With this system, all above NIR-II information is intuitively and accurately presented on visible image layer.

2.4 Dual-channel guided popliteal LN

We performed popliteal LN dissection in a rat to validate the practical feasibility of the dual-channel imaging system for surgical navigation. Prior to imaging, the popliteal LN was labeled by injecting ICG solution into the hind paw pad. As shown in Fig. 5a, the fluorescence clearly indicates the LN's location with skin intact, while the RGB image provides overall biological context. This system allows the surgeon to perform surgery without frequently looking down at the surgical field, significantly improving the surgical efficiency. After the initial exposure, while surrounded by adipose tissue and difficult to distinguish by the naked eye, the LN was clearly delineated in the merged image (Fig. 5b). The LN was then successfully dissected with the real-time dual-channel imaging guidance. After surgery, the fluorescence signal at the wound site nearly vanished (Fig. 5c). As shown in Fig. 5d, the excised LN exhibited significantly higher brightness than normal tissue. Thanks to the precise navigation, only a small amount of normal tissue attached to the excised LN, minimizing iatrogenic injury.

2.5 Blood supply assessment of reconstructed flap in patient

After suffering a sudden external force, the skin might be seriously peeled back, resulting in a degloving injury. It can expose underlying bone and muscle, significantly increasing the risk of infection. Flap reconstruction is a common repair method, but it carries a risk of tissue necrosis due to potential insufficient blood supply. In our previous work, we have demonstrated that NIR-II fluorescence imaging helps to fully assess blood supply condition of reconstructed human flap. However, such single-channel imaging technique presents challenges in accurately correlating fluorescent regions with anatomical structures.

Herein, we introduced our dual-channel imaging system into the operating room (Fig. 6a). A patient with a degloving injury on the dorsum of the left foot was enrolled. Due to severe soft tissue contusion, the patient underwent thorough debridement, followed by replantation of the degloved dorsal skin flap. One-week post-surgery, black necrosis at the edge of the flap was visually observed (Fig. 6b). However, the blood supply recovery in the superficial and deep flap may not be consistent. To accurately assess blood supply recovery of the deep layer and identify specific necrotic foci, we administered an intravenous injection of ICG (2.5 mg/mL, 3 mL) and performed dual-channel imaging. Fluorescence of blood vessels in the foot dorsum appeared 45 seconds after injection approximately. Figs. 6c and d show the merged images captured 1.5 and 4.5 minutes post-injec-

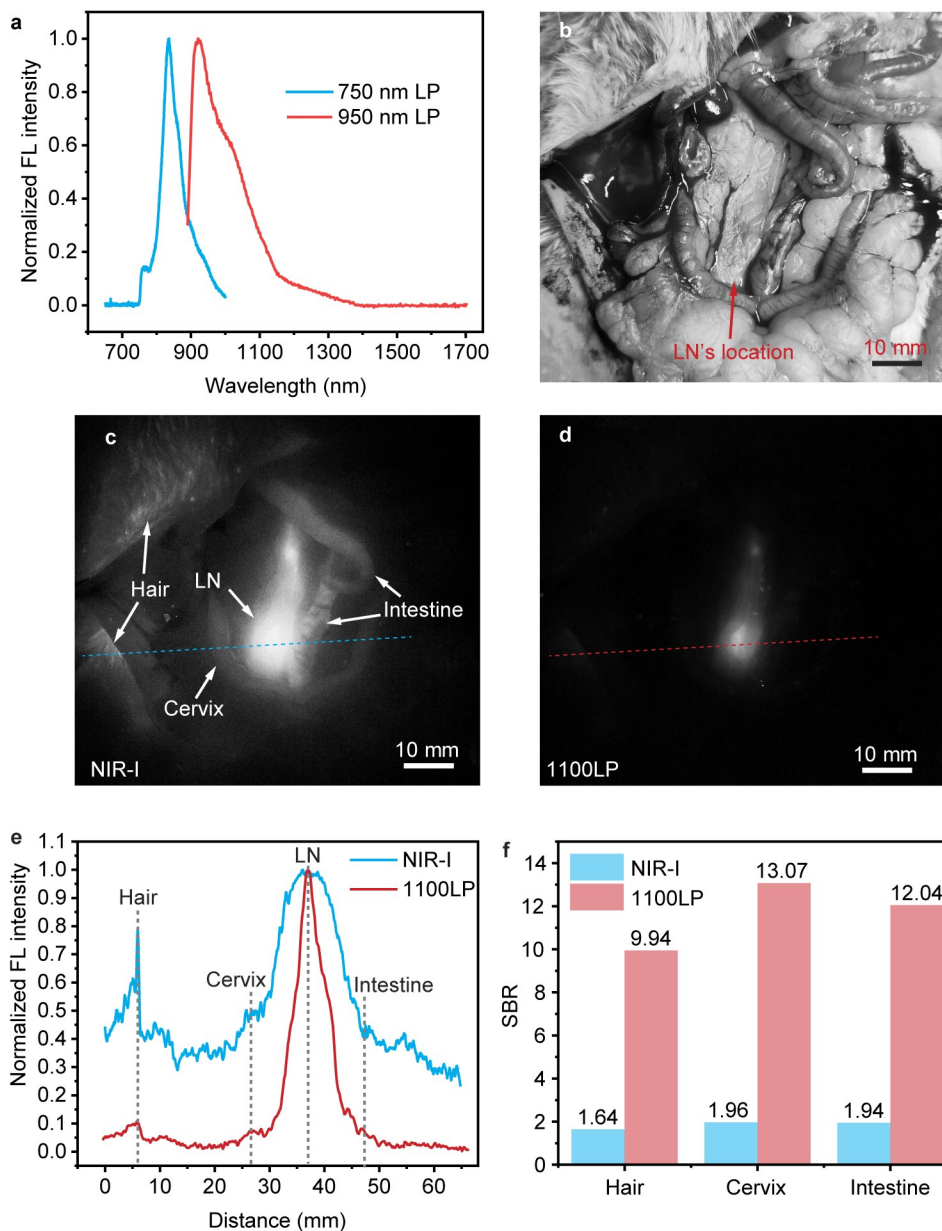


图1 可见光、NIR-I 荧光和 NIR-II 荧光成像的对比:(a) ICG的发射光谱。受限于光谱仪的灵敏度范围,光谱分为两部分测量和展示。蓝色曲线由硅基光谱仪检测(激发波长:665 nm 激光,滤光片:750 nm LP),红色曲线由砷化镓光谱仪测量(激发波长:808 nm 激光,滤光片:950 nm LP);大鼠腹膜后区域的(b)可见光、(c)NIR-I 和(d)NIR-II 图像。腹膜后淋巴结使用 ICG 进行标记。NIR-I 图像是使用硅基相机、700 nm LP 和 900 nm SP 滤光片拍摄的,而近红外-II 图像是使用砷化镓相机和 1100 nm LP 滤光片拍摄的;(e)沿(c)和(d)中虚线的归一化强度曲线;(f)根据(e)计算的 SBR。将淋巴结的强度峰值作为信号,而头发、子宫和肠道的强度作为背景。与 NIR-I 相比,NIR-II 图像(命名为 1100LP)显示出明显更高的 SBR,可提供更可靠的淋巴结识别

Fig. 1 Comparison of visible light imaging, NIR-I and NIR-II fluorescence imaging: (a) Emission spectrum of ICG. Due to the limitations of spectrometers' sensitivity range, the spectrum is presented in two parts. The blue curve was detected by a silicon-based spectrometer (excitation: 665 nm laser, filter: 750 nm LP), while the red curve was measured by an InGaAs-based spectrometer (excitation: 808 nm laser, filter: 950 nm LP). (b) Visible light, (c) NIR-I, and (d) NIR-II images of the rat retroperitoneal region. The retroperitoneal LN was labeled by ICG. The NIR-I image was captured using a silicon-based camera, a 700 nm LP filter, and a 900 nm SP filter, while the NIR-II image was captured using an InGaAs-based camera and a 1100 nm LP filter. (e) Normalized intensity profiles along the dashed lines in (c) and (d). (f) Calculated SBRs from (e). The intensity peak of the LN was taken as signal, while the intensity of hair, cervix, and intestine served as backgrounds. The NIR-II image (named 1100LP) shows a significantly higher SBR compared to NIR-I, making LN identification more reliable

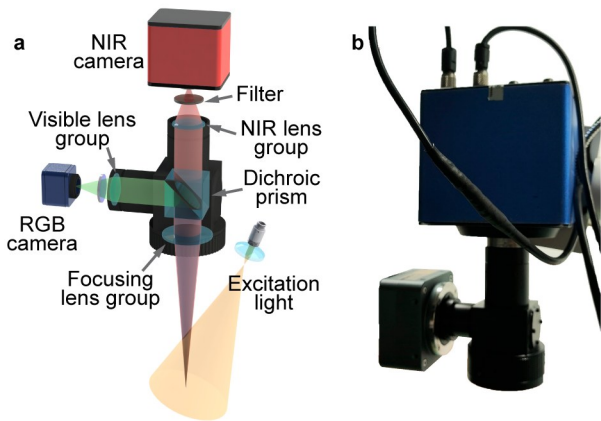


图2 共轴可见光与NIR-II双通道成像系统:(a)光学结构的示意图。该系统由激光光源、RGB相机、NIR-II相机、共轴双通道镜头和滤光片组成。共轴双通道镜头可以从相同视角同时进行可见光和NIR-II成像;(b)实际成像系统的照片

Fig. 2 Coaxial visible and NIR-II dual-channel imaging system: (a) Schematic diagram of the optical setup. The system consists of an excitation light source, RGB camera, NIR-II camera, coaxial dual-channel lens, and filters. The coaxial dual-channel lens allows both visible and NIR-II imaging from the same perspective. (b) Photograph of the actual imaging system

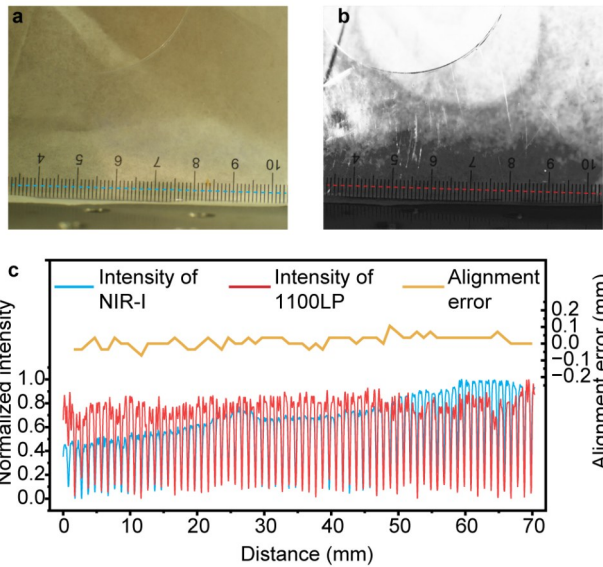


图3 两个通道之间对准误差的表征:系统拍摄的标尺的(a)RGB图像和(b)1100LP图像,成像时使用卤素灯作为光源;(c)沿着(a)和(b)中虚线的强度的归一化曲线。曲线的谷值对应于刻度线的位置。图(c)中还显示了两个通道中对应谷值(刻度线)之间的距离

Fig. 3 Characterization of alignment error between the two channels: (a) RGB and (b) 1100LP images of a ruler taken by the system with a halogen lamp as the illumination source. (c) Normalized intensity profiles across the dashed lines in (a) and (b). The valleys of the curves correspond to the positions of scale lines. The distances between corresponding valleys (scale lines) in the two channels are also shown in (c)

tion, respectively. The merged images reveal that the skin at the flap edge remained black without obvious vascular filling (see area marked in yellow dashed line in Fig. 6c), while small vessels were gradually observed crawling and filling at the medial edge over time (Fig. 6d), suggesting possible neovascularization.

This ICG-based NIR-II and visible light dual-channel imaging system provided clinicians with intuitive and valuable information regarding the blood supply status of the traumatic flap and potential neovascularization. This information serves as a crucial reference for the patient's future treatment decisions, such as whether to proceed with further debridement or continue observation.

3 Conclusions

In this study, we developed a coaxial dual-channel imaging system for visible light and NIR-II fluorescence. The alignment error between the two channels was minimized to within ± 0.15 mm, and the system achieved high resolution, capable of visualizing vessels as thin as 0.44 mm. It was successfully applied to dual-channel-guided rat LN excision and human flap survival assessment, significantly improving surgical efficiency and diagnostic accuracy. Future enhancements could further expand the system's capabilities. Replacing the laser excitation source with LEDs might improve safety and portability, and incorporating a zoom function could better accommodate various imaging needs.

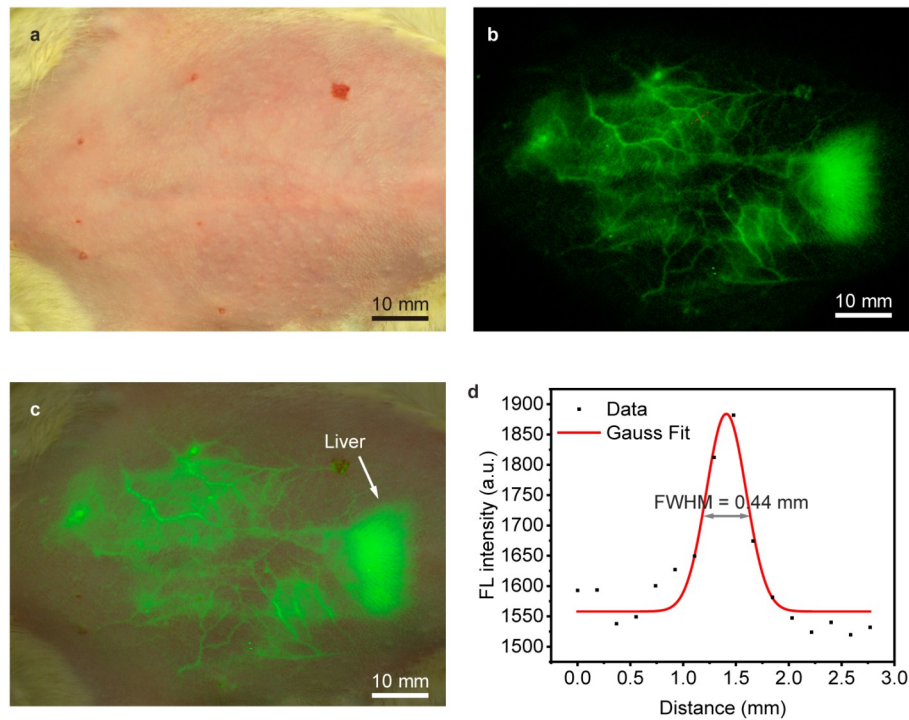


图4 大鼠腹部血管的双通道成像将0.5 mL浓度为2 mg/mL的ICG溶液注射到大鼠的静脉中以标记血管。大鼠腹部的(a)RGB图像、(b)1100LP荧光图像和(c)合成图像。1100LP荧光图像显示了肝脏形态和血管网络的丰富细节;(d)沿着(b)中红色虚线的强度分布,可分辨出一条半高全宽仅为0.44 mm的细血管。激发光源:808 nm CW激光,功率密度:140 mW/cm²。FL: fluorescence: Rats were injected with 0.5 mL of 2 mg/mL ICG solution into the vein to label blood vessels. (a) RGB image, (b) 1100LP fluorescence image, and (c) merged image of the rat abdomen. The 1100LP fluorescence image shows liver morphology and vascular network with high details. (d) Intensity profile along the red dashed line in (b), resolving a thin blood vessel with a FWHM of only 0.44 mm. Excitation: 808 nm CW laser, power density: 140 mW/cm². FL: fluorescence

Fig. 4 Dual-channel imaging of rat abdominal blood vessels

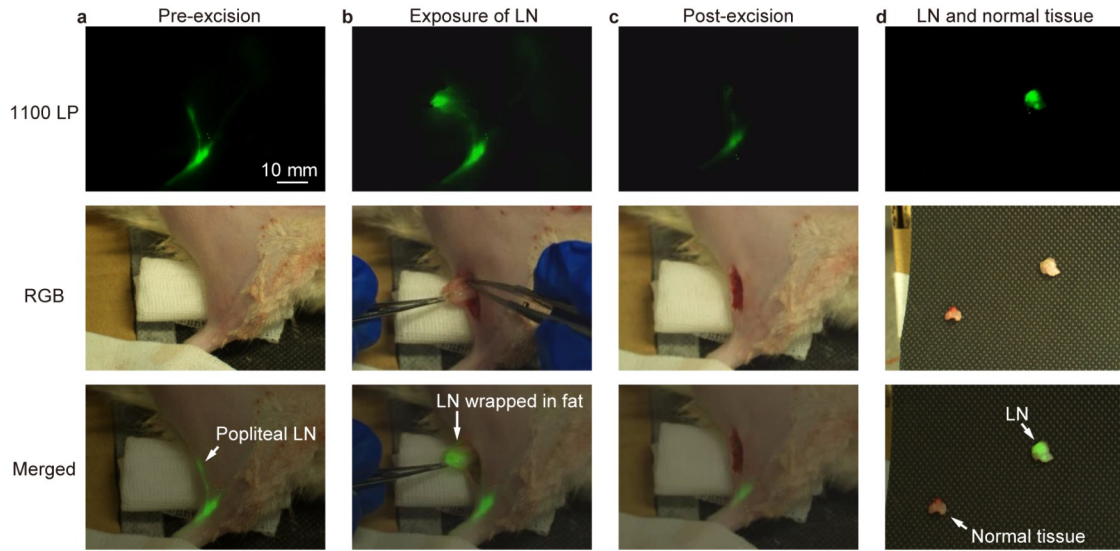


图5 双通道引导下的大鼠腘窝淋巴结切除实验前,将0.25 mL浓度为1 mg/mL的ICG溶液注射到大鼠后爪垫,以标记腘窝淋巴结。(a) 切除前的大鼠后腿图像。荧光清晰地显示了腘窝淋巴结和淋巴管的位置;(b) 术中图像。可见腘窝淋巴结被白色脂肪组织包围,但在融合图像中清晰可辨;(c) 切除后的后腿图像。切口处荧光信号几乎消失;(d) 淋巴结和正常组织的图像。淋巴结显示出明亮的荧光,而正常组织的信号强度则为背景水平。精准的淋巴结切除使得对周围正常组织的损伤最小化。激发光源:808 nm CW激光,功率密度为20 mW/cm²;Prior to the experiment, the rat was injected with 0.25 mL of 1 mg/mL ICG solution into the hind paw pad to label the popliteal LN. (a) Image of the rat hind leg before resection. Fluorescence clearly indicates the position of the popliteal LN and lymphatic vessels. (b) Intraoperative image. The LN, enclosed in white adipose tissue, was clearly delineated in merged image. (c) Post-excision image of the leg. The fluorescence signal in the wound site has almost disappeared. (d) Images of LN and normal tissue. The LN exhibits strong fluorescence, while normal tissue shows background-level intensity. Precise LN excision minimizes damage to the surrounding normal tissue. Excitation: 808 nm CW laser, with a power density of 20 mW/cm²

Fig. 5 Dual-channel-guided rat popliteal LN resection



图6 皮瓣重建手术后1周的血供评估(a)手术室内的系统照片;(b)脚部的RGB图像。可见皮瓣边缘有黑色坏死;注射ICG(浓度为2.5 mg/mL,3 mL)后(c)1.5分钟和(d)4.5分钟左右拍摄的NIR-II荧光和RGB融合图像。在皮瓣边缘(由黄色虚线圈出)未观察到荧光信号,表明血供不足。在白色虚线标记区域内则逐渐出现荧光,提示可能有微小血管形成。(a) System setup in the operating room. (b) RGB image of the foot, showing black necrosis at the flap edge. Merged NIR-II and RGB images captured at about (c) 1.5 minutes and (d) 4.5 minutes post-injection of ICG (2.5 mg/mL, 3 mL). No fluorescence signal is observed at the flap edge (marked by the yellow dashed line), indicating insufficient blood supply. Gradual fluorescence emergencies seen within the area marked by the white dashed line, suggesting the possible formation of small blood vessels.

Fig. 6 Blood supply assessment one week after flap reconstructive surgery

References

- [1] WANG X, TEH C S C, ISHIZAWA T, *et al.* Consensus Guidelines for the Use of Fluorescence Imaging in Hepatobiliary Surgery [J]. *Annals of Surgery*, 2021, **274**(1).
- [2] VAN MANEN L, HANDGRAAF H J M, DIANA M, *et al.* A practical guide for the use of indocyanine green and methylene blue in fluorescence-guided abdominal surgery [J]. *Journal of Surgical Oncology*, 2018, **118**(2): 283–300.
- [3] WANG K, DU Y, ZHANG Z, *et al.* Fluorescence image-guided tumour surgery [J]. *Nature Reviews Bioengineering*, 2023, **1**(3): 161–79.
- [4] DIP F, BONI L, BOUVET M, *et al.* Consensus Conference Statement on the General Use of Near-infrared Fluorescence Imaging and Indocyanine Green Guided Surgery: Results of a Modified Delphi Study [J]. *Annals of Surgery*, 2022, **275**(4).
- [5] MATSUI A, TANAKA E, CHOI H S, *et al.* Real-time intra-operative near-infrared fluorescence identification of the extrahepatic bile ducts using clinically available contrast agents [J]. *Surgery*, 2010, **148**(1): 87–95.
- [6] TANAKA E, CHEN F Y, FLAUMENHAFT R, *et al.* Real-time assessment of cardiac perfusion, coronary angiography, and acute intravascular thrombi using dual-channel near-infrared fluorescence imaging [J]. *The Journal of Thoracic and Cardiovascular Surgery*, 2009, **138**(1): 133–40.
- [7] VAN DER VORST J R, SCHAAFSMA B E, HUTTEMAN M, *et al.* Near-infrared fluorescence-guided resection of colorectal liver metastases [J]. *Cancer*, 2013, **119**(18): 3411–8.
- [8] CURRIE A C, BRIGIC A, THOMAS-GIBSON S, *et al.* A pilot study to assess near infrared laparoscopy with indocyanine green (ICG) for intraoperative sentinel lymph node mapping in early cancer [J]. *European Journal of Surgical Oncology*, 2017, **43**(11): 2044–51.
- [9] BURROWS P E, GONZALEZ-GARAY M L, RASMUSSEN J C, *et al.* Lymphatic abnormalities are associated with RASA1 gene mutations in mouse and man [J]. *Proceedings of the National Academy of Sciences*, 2013, **110**(21): 8621–6.
- [10] ROSENTHAL E L, WARRAM J M, DE BOER E, *et al.* Safety and Tumor Specificity of Cetuximab-IRDye800 for Surgical Navigation in Head and Neck Cancer [J]. *Clinical Cancer Research*, 2015, **21**(16): 3658–66.
- [11] DIAO S, HONG G, ANTARIS A L, *et al.* Biological imaging without autofluorescence in the second near-infrared region [J]. *Nano Research*, 2015, **8**(9): 3027–34.
- [12] FAN X, YANG J, NI H, *et al.* Initial Experience of NIR-II Fluorescence Imaging-Guided Surgery in Foot and Ankle Surgery [J]. *Engineering*, 2024, **40**: 19–27.
- [13] HONG G, ANTARIS A L, DAI H. Near-infrared fluorophores for biomedical imaging [J]. *Nature Biomedical Engineering*, 2017, **1**(1): 0010.
- [14] FENG Z, TANG T, WU T, *et al.* Perfecting and extending the near-infrared imaging window [J]. *Light: Science & Applications*, 2021, **10**(1): 197.
- [15] FENG Z, YU X, JIANG M, *et al.* Excretable IR-820 for in vivo NIR-II fluorescence cerebrovascular imaging and photothermal therapy of subcutaneous tumor [J]. *Theranostics*, 2019, **9**(19): 5706–19.
- [16] FENG Z, BAI S, QI J, *et al.* Biologically Excretable Aggregation-Induced Emission Dots for Visualizing Through the Marmosets Intravascularly: Horizons in Future Clinical Nanomedicine [J]. *Advanced Materials*, 2021, **33**(17): 2008123.
- [17] WELSHER K, LIU Z, SHERLOCK S P, *et al.* A route to brightly fluorescent carbon nanotubes for near-infrared imaging in mice [J]. *Nature Nanotechnology*, 2009, **4**(11): 773–80.
- [18] ZHANG Y, ZHOU J, PENG S, *et al.* Hot-Band-Absorption-Induced Anti-Stokes Fluorescence of Aggregation-Induced Emission Dots and the Influence on the Nonlinear Optical Effect [J/OL] 2021, **11**(11): 10.3390/bios11110468
- [19] ZHOU H, LU Z, ZHANG Y, *et al.* Simultaneous Enhancement of the Long-Wavelength NIR-II Brightness and Photothermal Performance of Semiconducting Polymer Nanoparticles [J]. *ACS Applied Materials & Interfaces*, 2022, **14**(7): 8705–17.
- [20] FAN X, XIA Q, ZHANG Y, *et al.* Aggregation-Induced Emission (AIE) Nanoparticles-Assisted NIR-II Fluorescence Imaging-Guided Diagnosis and Surgery for Inflammatory Bowel Disease (IBD) [J]. *Advanced Healthcare Materials*, 2021, **10**(24): 2101043.
- [21] FAN X, LI Y, FENG Z, *et al.* Nanoprobes-Assisted Multichannel NIR-II Fluorescence Imaging-Guided Resection and Photothermal Ablation of Lymph Nodes [J]. *Advanced Science*, 2021, **8**(9): 2003972.
- [22] ZHANG Z, DU Y, SHI X, *et al.* NIR-II light in clinical oncology: opportunities and challenges [J]. *Nature Reviews Clinical Oncology*, 2024, **21**(6): 449–67.
- [23] HU S, FANG C, LI B, *et al.* First-in-human liver-tumour surgery guided by multispectral fluorescence imaging in the visible and near-infrared-I/II windows [J]. *Nature Biomedical Engineering*, 2020, **4**(3): 259–71.
- [24] QU Q, NIE H, HOU S, *et al.* Visualisation of pelvic autonomic nerves using NIR-II fluorescence imaging [J]. *European Journal of Nuclear Medicine and Molecular Imaging*, 2022, **49**(13): 4752–4.
- [25] CAO C, JIN Z, SHI X, *et al.* First Clinical Investigation of Near-Infrared Window IIa/IIb Fluorescence Imaging for Precise Surgical Resection of Gliomas [J]. *IEEE Transactions on Biomedical Engineering*, 2022, **69**(8): 2404–13.
- [26] FAN X, XIA Q, LIU S, *et al.* NIR-II and visible fluorescence hybrid imaging-guided surgery via aggregation-induced emission fluorophores cocktails [J]. *Materials Today Bio*, 2022, **16**: 100399.
- [27] 刘雯, 倪沪桅, 钱骏. 可见-近红外二区双通道荧光成像系统 [J]. *红外与毫米波学报*, **43**(3): 415–22.
- [28] ROUVAS A A, PAPAKOSTAS T D, NTOURAKI A, *et al.* Angiographic and OCT features of retinal angiomatous proliferation [J]. *Eye*, 2010, **24**(11): 1633–43.

-
- [29] JØRGENSEN M G, HERMANN A P, MADSEN A R, *et al.* Indocyanine green lymphangiography is superior to clinical staging in breast cancer-related lymphedema [J]. *Scientific Reports*, 2021, **11**(1): 21103.
- [30] TENG C W, HUANG V, ARGUELLES G R, *et al.* Applications of indocyanine green in brain tumor surgery: review of clinical evidence and emerging technologies [J]. *Neurosurgical Focus FOC*, 2021, **50**(1): E4.
- [31] RAABE A, BECK J, GERLACH R, *et al.* Near-infrared Indocyanine Green Video Angiography: A New Method for Intraoperative Assessment of Vascular Flow [J]. *Neurosurgery*, 2003, **52**(1).
- [32] CHERRICK G R, STEIN S W, LEEVY C M, *et al.* INDOCYANINE GREEN: OBSERVATIONS ON ITS PHYSICAL PROPERTIES, PLASMA DECAY, AND HEPATIC EXTRACTION [J]. *The Journal of Clinical Investigation*, 1960, **39**(4): 592-600.